Effect of Flow Field Heterogeneity in Coagulators on Aggregate Size and Structure

Lyonel Ehrl, Miroslav Soos, Hua Wu, and Massimo Morbidelli
Dept. of Chemistry and Applied Biosciences, Institute for Chemical and Bioengineering, ETH Zurich, 8093 Zurich, Switzerland

DOI 10.1002/aic.12179
Published online January 13, 2010 in Wiley Online Library (wileyonlinelibrary.com).

Aggregate size and structure were investigated under turbulent conditions in stirred tank (ST) and Taylor–Couette-type (TC-type) devices. Root-mean-square radius of gyration, $\langle \mathrm{Rg} \rangle$, and zero-angle intensity of scattered light, I(0), were acquired as a function of stirring intensity, characterized by an experimentally obtained average hydrodynamic stress, $\langle \tau \rangle_{\mathrm{exp}}$, determined by torque measurements. Evaluating aggregate images revealed that aggregate structure and shape are independent of the device type. However, in TC-type devices, the aggregates grow to three to four times larger sizes than inside ST, although the same $\langle \tau \rangle_{\mathrm{exp}}$ was used in both coagulators. As confirmed by computational fluid dynamics, this can be attributed to the differences in the maximum hydrodynamic stress in ST compared with those in TC-type devices. In contrast, the power-law scaling of $\langle \mathrm{Rg} \rangle$ and I(0) with $\langle \tau \rangle_{\mathrm{exp}}$ is preserved for all investigated devices, with an exponent approximately equal to −0.5 and −0.7, respectively.
 AIChE J, 56: 2573–2587, 2010
Keywords: aggregation/breakage, stirred tank, lobed Taylor–Couette, hydrodynamic stress distribution, steady-state reversibility

Introduction

The separation of fine particles from dispersions is essential to many industrial processes, for example, water treatment[1] and postprocessing in emulsion polymerization.[2] This can be achieved by destabilizing the dispersions with coagulant and subsequent stirring to aggregate the particles to form larger clusters that can be separated more easily. During this procedure, usually two processes are present, that is, aggregation and breakage, both dependent on applied shear rate or stirring speed. In the literature, various studies exist addressing the effect of the stirring intensity on the aggregation kinetics, the aggregate size and structure, however, using single devices.[3–15] In these studies, the resulting aggregate populations are analyzed assuming homogeneous flow conditions, where the volume average shear rate, $\langle G \rangle = \sqrt{\langle \varepsilon \rangle / \nu}$, obtained from the power input usually serves as the characteristic quantity of the flow field. However, in reality for a given stirring device, the shear rate exhibits a distinct distribution.[16–25] As the rate constants of both aggregation[26–28] and breakage[29] are not linearly dependent on shear rate, its volume average value cannot be used to properly characterize these processes, but the heterogeneity of the flow field needs to be considered.[30,31] Therefore, reducing the considerations on $\langle G \rangle$ can lead to erroneous results in the scale-up, and it complicates the comparison of different stirring/mixing devices. We note that this picture[26–31] is in contrast to the classical view of aggregation being linearly dependent on shear as introduced by von Smoluchowski.[32] By combining population balance equations with computational fluid dynamics (CFD), Marchisio et al.[30,31] showed that the homogeneous approach is only valid for very low solid volume fractions, apart from that the local quantities of the shear rate need to be considered. Besides theoretical considerations, by applying compartment models in combination with population balance equations for stirred tank (ST)[33–35] and Taylor–Couette (TC) geometries[36] or quadrature method

Additional Supporting Information may be found in the online version of this article.

Correspondence concerning this article should be addressed to M. Morbidelli at massimo.morbidelli@chem.ethz.ch.

of moments in combination with CFD,[13,15,30,31] to our knowledge, there are rather few experimental works[16,37–39] dedicated to the effect of the flow field heterogeneity on aggregation and breakage processes moreover with contradicting results. Ducoste et al.[37] compared STs of various sizes and equipped with different impellers. They found that for constant $\langle G \rangle$ the aggregate size distribution shifts to smaller sizes coming from an axial (A310 fluid foil) to a radial impeller (Rushton turbine). Similar results obtained by the same authors were collected for increasing tank size operated at constant $\langle G \rangle$. This is explained by the fact that to maintain a constant $\langle G \rangle$ when increasing the tank size, the turbulent intensity in the discharge zone increases and also aggregate breakup increases. In contrast, for a ST, Spicer et al.[38] investigated the effect of impeller type on the aggregate size and structure and found no considerable influence on both of these quantities. Coufort et al.[16] studied the irreversible aggregation of bentonite in a TC reactor and in a jar. For the same volume average energy dissipation rate, $\langle \varepsilon \rangle$, they observed larger aggregate sizes inside the TC reactor compared with the jar, whereas the scaling of the aggregate size with $\langle \varepsilon \rangle$ was the same for both devices with an exponent equal to -0.25. They attributed the difference in aggregate size to the difference in the distributions of the energy dissipation rate, that is, they showed that the mode (most probable value) of the aggregate size distribution correlates with the mode of the energy dissipation rate distribution. In two separate works, without discussing the effect of flow field heterogeneity, Selomulya et al. reported data obtained within a ST[11] and a TC reactor[12] using polystyrene particles with diameter of 380 nm at a solid volume fraction of 3.8×10^{-5}. Comparing the data for similar $\langle G \rangle$, they obtain aggregate sizes (twice the radius of gyration) inside the ST three times larger than inside the TC, which is in contrast to the results of Coufort et al.[16] Even more striking is the substantial variation of the scaling exponent, used as a measure of the aggregate compactness, with values from 1.8 to 2.3 for ST and between 2.5 and 3.0 for TC, although both devices were operated under turbulent conditions. Recently, Serra et al.[39] reported aggregation experiments for one colloidal system in various devices for low shear rates. Here, a nonmonotonical dependency of the steady-state aggregate size with $\langle G \rangle$ in the range from 4 to 102 s^{-1} with a maximum at $20\ s^{-1} < \langle G \rangle < 30\ s^{-1}$ was observed. In their work, the aggregates grew to larger sizes inside the TC device compared with a paddle mixer and an oscillating grid reactor, with scaling proportionality between aggregate size and shear rate, which is different for each device. Also, the values of the aggregates fractal dimension obtained for each device differ. For the behavior of all obtained quantities, the maximum in aggregate size, the different size-shear rate proportionalities, and the different fractal dimensions, no clear explanation is given.

Besides studies on aggregation and breakage processes, because of the growing field of bioengineering and its applications, interest is raised in the effect of shear on fermentation processes[40–42] and the fluid dynamics in fermentation equipment.[43] As a result of these studies, devices different from standard STs are considered.[40,42,44,45]

Therefore, the main objective of this work is to investigate the effect of the flow field heterogeneity on the steady-state size and structure of aggregates. To do so, mixing devices with substantially different distributions of the shear rate (or hydrodynamic stress) will be used, in particular, a ST equipped with a Rushton turbine, and TC-type of devices. In this way, the relative difference of the stresses affecting the dynamic equilibrium between aggregation and breakage can be determined experimentally.

This article is organized as follows. The applied experimental materials and methodology as well as the measurement methods used to characterize the size and structure of the formed aggregates, the flow field visualization, and the torque measurement are presented in Section "Materials, Methodology, and Measurement Methods". Further, this section also includes a discussion on the CFD methods used to simulate the flow field and to calculate the hydrodynamic stresses inside the studied coagulators. In Section "Results and Discussion". first, the effect of the inner cylinder deformation on the instability of the flow field in TC devices is discussed. Second, the data obtained from aggregation and breakage experiments are introduced and discussed with respect to the reversibility of steady-state aggregate properties (e.g., aggregate size and structure). Third, the scaling of the steady-state aggregate properties obtained in various stirring devices with respect to hydrodynamic stress is compared. In Conclusion, the work and main findings are summarized.

Materials, Methodology, and Measurement Methods

Stirring devices and fluid flow characterization

The experiments were performed with three TC-type devices and with a ST. The three TC-type devices varied in cross-section geometry of their inner rotating cylinders, where one was circular, resulting in a classical TC with a gap width of 8 mm, and the other two were triangular shaped with increasing maximum gap of 12 and 20 mm, from hereon called lobed Taylor–Couette (LTC) devices. The cross sections of the fluid volume enclosed by the inner and outer cylinder for the three TC-type devices are shown in Figure 1, and hence the devices will be named TC 8, LTC 8–12, and LTC 8–20. For the TC 8 and the LTC 8–12, the inner cylinder is made from polished stainless steel and for the LTC 8–20 from polyvinyl chloride. Two types of outer cylinder were used in the experiments, one made from stainless steel with several sampling ports, and the other from precision glass Duran from Schott (Mainz, Germany) used for flow field visualization with rheoscopic fluid. More details about the geometry of the coagulation units as well as on the characterization of the flow field through CFD can be found in Soos et al.[17] for the TC-type devices, and Waldner et al.[14] and Soos et al.[46] for the ST, respectively.

Characterization of Flow Conditions and Flow Field Visualization. For the aggregation experiments, the TC-type devices were operated with stirring speeds in the range from 200 to 1200 rpm, and the ST was operated in the range from 200 to 1000 rpm. To characterize the flow inside the TC-type devices, the following definition for the inner cylinder Reynolds number,[47,48] $\mathrm{Re}_{\mathrm{cyl}}$, relating inertial forces relative to viscous forces, and the inner cylinder Taylor number,[48]

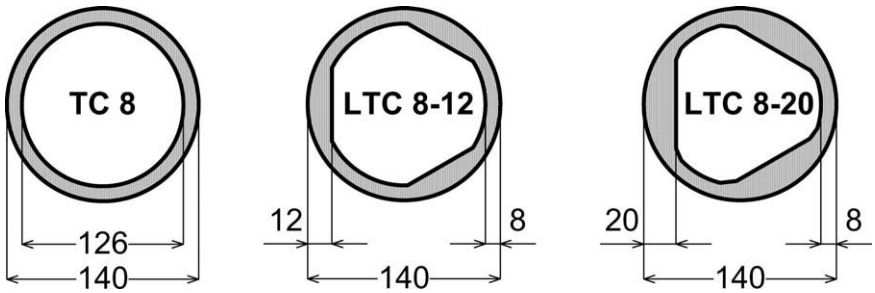

Figure 1. Cross section of fluid volume (hatched areas) enclosed by the inner and outer cylinder for the classical TC (TC 8) and the two lobed TC devices (LTC 8–12 and LTC 8–20).

Dimensions are in mm.

Ta_{cyl}, relating centrifugal forces relative to viscous forces, are used:

$$Re_{cyl} = \frac{r_i \omega_i d_{gap}}{\nu} \tag{1}$$

$$Ta_{cyl} = \frac{r_i \omega_i^2 d_{gap}^3}{\nu^2} = Re_{cyl} \frac{\omega_i d_{gap}^2}{\nu} \tag{2}$$

Here d_{gap} is the difference between the outer and the inner radii, r_o and r_i, enclosing the fluid volume, $\omega_i = 2\pi N/60$ is the angular velocity of the inner cylinder with N being the number of rotations per minute, and ν is the kinematic viscosity (for water at 25°C approximately equal to 10^{-6} m^2 s^{-1}). The flow pattern inside a TC can be related to the ratio between Re_{cyl} and a critical Reynolds number,[48] Re_{cri} (or equivalently Ta_{cyl} and Ta_{cri}), which characterizes conditions when the flow in the annular gap changes from purely laminar circular Couette flow to the Taylor vortex flow characterized by the presence of axisymmetric toroidal vortices. This transition is also dependent on the ratio of the inner and outer cylinder radii. Therefore, Re_{cri} (or Ta_{cri}) has to be measured experimentally, or it can be determined from correlations presented in the literature. For example, by using the following correlation provided by Taylor[49]:

$$Ta_{cri} = \frac{\pi^4 (1 + d_{gap}/2r_i)}{0.0571(1-0.652 d_{gap}/r_i) + 0.00056(1-0.652 d_{gap}/r_i)^{-1}} \tag{3}$$

and the geometry of the TC 8 device Ta_{cri} and corresponding $Re_{cri} = (Ta_{cri}\nu)/(\omega_i d_{gap}^2)$ are equal to 1953 and 123, respectively, which is in agreement with Andereck et al.[47] and Lueptov et al.[50] In the case of LTC 8–12 and LTC 8–20, because of the nonconstant gap width the transition from Couette to Taylor vortex flow in the annular gap can be characterized by two critical Taylor numbers $Ta_{cri,min}$ and $Ta_{cri,max}$ (from $Ta_{cyl,min}$ and $Ta_{cyl,max}$) or consequently two critical Reynolds numbers $Re_{cri,min}$ and $Re_{cri,max}$ (from $Re_{cyl,min}$ and $Re_{cyl,max}$). In this work it was found that the transition from the circular Couette flow to the Taylor vortex flow is controlled by the larger gap, with $Ta_{cri,max}$ equal to 2134 and 2682 (and $Re_{cri,max}$ equal to 102 and 82) for LTC 8–12 and LTC 8–20, respectively. For the visualization of the flow structure, the TC-type devices mounted with the glass outer cylinder were filled with a ready-to-use rheoscopic fluid AQ-RF from Kalliroscope Corporation (Groton, MA). As it was shown that the flow pattern in TC-type devices for various ratios of r_i/r_o can be characterized by $Re_{cyl,max}/Re_{cri,max}$,[48,50] same method will be applied also in this work.

In a similar manner as in TC-type devices, the flow inside the ST is characterized by an impeller Reynolds number, Re_{imp}, according to[51]:

$$Re_{imp} = \frac{(N/60) d_{imp}^2}{\nu}. \tag{4}$$

Here, d_{imp} is the impeller diameter. The Reynolds numbers resulting from Eqs. 1 and 4 applied during the aggregation experiments for the various devices are listed in Table 1.

Torque Measurement, Hydrodynamic Stresses, and Computational Fluid Dynamics. For TC-type devices, the flow was further characterized through torque measurements[52–54] in the following way. The net torque, T, was determined from the difference in the torques on the inner

Table 1. Dimensions and Operation Conditions of the Coagulation Units

Device Type	d_{min}/mm	d_{max}/mm	V/L	N/(1/min)	$Re_{cyl,min}$/(−)	$Re_{cyl,max}$/(−)
TC 8	8		1.35	[200;1200]	[1.0;62] × 10^4	
LTC 8–12	8	12	1.50	[200;1200]	[1.0;62] ×10^4	[1.5;87] ×10^4
LTC 8–20	8	20	1.99	[200;1200]	[1.0;62] ×10^4	[2.1;126] ×10^4
Device Type	d_{tank}/mm	d_{imp}/mm	V/L	N/(1/min)	Re_{imp}/(−)	
ST	140	60	2.57	[200;1000]	[1.2;60] × 10^4	

d_{min} and d_{max} are the minimum and maximum gap width, respectively, d_{tank} is the inner diameter of the ST, d_{imp} is the impeller diameter, V is the total fluid volume, N are the rotations per minute applied in the aggregation experiments, and the corresponding Reynolds numbers are calculated according to Eqs. 1 (Re_{cyl},min and Re_{cyl},max) and 4 (Re_{imp}).

cylinder for the coagulation unit with and without water at various stirring speeds. For this, a torque meter MCRT28001T-25-0-NA from Himmelstein & Company (Hoffman Estates, IL) was used. From T, the volume average rate of dissipated energy, $\langle\varepsilon\rangle$, can be calculated according to

$$\langle\varepsilon\rangle = \frac{\omega_i T}{V}, \tag{5}$$

where V is the reactor volume. Consequently, these values were used to evaluate an experimentally obtained average hydrodynamic stress $\langle\tau\rangle_{exp} = \mu\sqrt{\langle\varepsilon\rangle/\nu}$.

Aggregate breakup occurs when the hydrodynamic stress exceeds the aggregate strength. Depending on the type of flow (laminar or turbulent) and relative size of the aggregates with respect to the characteristic size of the flow, there are various types of the hydrodynamic stress that have to be evaluated. The first contribution to the aggregate breakup could be due to the gradient of the mean flow for which the corresponding hydrodynamic stress can be evaluated as follows:[55]

$$\tau_L = \frac{5}{2}\mu\alpha_L, \tag{6}$$

where μ is the dynamic viscosity and α_L is the maximum positive eigenvalue of the rate of strain tensor. As the flow in all investigated devices is three-dimensional, the maximum positive eigenvalues of the rate of strain tensor, α_L, were evaluated numerically by applying the Householder reduction and the QL method[56] evaluated from CFD results using a user-defined function.[57]

As the flow in the annular gap becomes weakly or even fully turbulent, the energy dissipation rate, ε, becomes the quantity that determines the hydrodynamic stress caused by turbulence. For aggregates within the viscous subrange of turbulence, that is, aggregates smaller than the Kolmogorov microscale, defined as follows:

$$\eta_K = \left(\frac{\nu^3}{\varepsilon}\right)^{1/4}, \tag{7}$$

the corresponding hydrodynamic stress can be calculated as:[58]

$$\tau_{VS} = \frac{5}{2}\mu\sqrt{\frac{\varepsilon}{6\nu}} \approx \mu\sqrt{\frac{\varepsilon}{\nu}}. \tag{8}$$

When the aggregate size is larger than η_K, that is, when the aggregates are in the inertial subrange of turbulence, the hydrodynamic stress to which the aggregate is exposed results from the difference in the pressure acting on opposite sides of the aggregate,[59] that is, the dynamic pressure. Under these conditions, the corresponding hydrodynamic stress can be approximated as follows:[58]

$$\tau_{IS} = \rho(\varepsilon d_{agg})^{2/3}, \tag{9}$$

where ρ is the fluid density and d_{agg} is the aggregate diameter.

To evaluate the local hydrodynamic properties, the flow fields of all devices were characterized with CFD using the software package Fluent version 6.2 from Ansys (Canonsburg, PA).

The torque measurements described earlier can only be used to quantify the volume average energy dissipation rate. Therefore, CFD simulations of all studied devices were used to characterize the local values of the hydrodynamic stresses. Because of the vessel symmetry, all simulations for the TC-type devices were carried out using only one-half of the unit height. The computational grid contained 20 nodes in radial direction, 170 nodes in axial direction, and 420 nodes in the circumferential direction. Across the gap width, the nodes were distributed asymmetrically to properly resolve the local large gradients near the inner and outer walls. For each investigated rotation speed, the grid size was refined until a grid size–independent solution was obtained. To take into account turbulent flow in the TC-type devices, a Reynolds stress model[60] combined with a standard wall function was used. The rotation of the inner cylinder was considered by a rotating reference frame, by rotating the liquid adjacent to the inner cylinder wall at the same velocity as the latter, whereas the outer cylinder is treated as static.[61] As it was shown by several authors,[17,45,62] the Reynolds stress model combined with a standard wall function provides the best agreement of local mean velocity components obtained from CFD simulations with experimental data. Therefore, in this work, we confine to a macroscopic comparison of the measured and calculated net torque for TC-type devices.

The conditions in the ST for the whole range of studied rotation speeds were turbulent, with an impeller Reynolds number varying from 12,000 to 60,000, calculated according to Eq. 4. The mean flow field in the ST was calculated through the standard k–ε model[60] combined with a standard wall function. By comparison with experimental data, various authors[58,63,64] showed that the k–ε model is a reasonable choice for the characterization of the mean flow field under given conditions in ST. At this it is mentioned that with respect to other aspects, for example, position of the trailing vortices, the k–ε model is inappropriate. Here, it is noted that ε is a key parameter to characterize flow heterogeneity, as it is strongly varying in the flow field. For more details, especially on the distribution of ε inside STs, we refer to a few works out of the vast literature on this topic.[18–25] To simulate the rotation of the impeller, a sliding mesh approach was adopted. The grid size was refined until a grid size–independent solution was achieved, resulting in the number of elements being approximately equal to 4×10^5 for 200 rpm increasing up to $\sim 1 \times 10^6$ for 1000 rpm.

Although the adopted CFD method properly predicts the mean flow field quantities, the hydrodynamic stresses evaluated through Eqs. 6–9 should be perceived as order of magnitude estimates rather than absolute values. For a deeper analysis of the turbulent flow, it is advised to use more space-resolved and, therefore, computational intensive large eddy simulations.[23–25,65] Alternatively, for rather simple geometries such as TC units, numerical methods based on the solution of equations of motion of interaction particles, for example, vortex methods or smooth particle hydrodynamics, can be used.[66,67]

Colloidal system and aggregation experiments

In all experiments, a white sulfate polystyrene latexes supplied by Interfacial Dynamics Corporation (Portland, OR) (product 1-600, coefficient of variation = 5.2%, batch no:

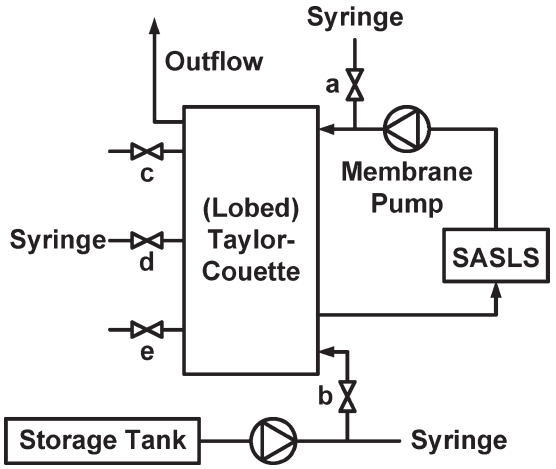

Figure 2. Schematic drawing of the experimental setup.

2042,1, solid % = 8.0%, and surface charge density = 3.9 μC/cm^2) were used. The mean diameter of the latex particles was equal to 600 nm, as measured by small-angle static light scattering, in agreement with the particle size declared by the producer. The measured particle size distributions are very narrow, and the latexes can be considered as monodisperse.

The initial suspension of primary particles with a solid volume fraction equal to 2×10^{-5} for all primary particle sizes was prepared by diluting the original latex with an appropriate amount of deionized water and subsequently pumped from a storage tank into the coagulation unit. A schema of the experimental setup of the TC-type devices is shown in Figure 2. An overflow tube was used as a small reservoir of about 100 mL to allow replenishing of the coagulation unit with liquid during sampling and to prevent air from entering the coagulator (see Figure 2). Then, the aggregation process was started by adding a coagulant solution (30 mL of 20% (w/w) $Al(NO_3)_3$ in water) using a syringe (see Figure 2, port a) and monitored until the system reached steady state with respect to the measured light scattering quantities. The resulting salt concentration was well above the critical coagulation concentration for the given system, that is, the electrostatic repulsive forces between the particles were fully screened, and the particles were completely destabilized. To achieve a good reproducibility for the salt injection and the off-line sampling, a programmable syringe pump, Vit-Fit (Lambda, Czechia), was used. For more details about the experimental procedure, we refer to our previous work for ST.[46,68–70]

Small-angle static light scattering and image analysis

A small-angle static light scattering instrument, Mastersizer 2000 (Malvern, UK), was used in all experiments for on-line characterization of the cluster mass distributions (CMDs) in the ST in terms of angle-dependent intensity of scattered light. This can be expressed as follows[71]:

$$I(q) = I(0)P(q)S(q), \tag{10}$$

where $I(0)$ is the zero-angle intensity of scattered light, $P(q)$ is the form factor (due to primary particles), and $S(q)$ is the structure factor (due to the arrangement of primary particles within the aggregates). The scattering vector amplitude, q, is defined as follows:

$$q = 4\pi \frac{n}{\lambda} \sin(\theta/2), \tag{11}$$

where θ is the scattering angle, n is the refractive index of the dispersing fluid, and λ is the laser wavelength in vacuum.

Analysis of the measured scattered intensity, $I(q)$, in the Guinier region (for qR_g up to about unity) allows one to extract two characteristic quantities of the CMD, namely the root-mean-square (rms) radius of gyration, $\langle R_g \rangle = \sqrt{\langle R_g^2 \rangle}$, and the absolute zero-angle intensity, $I(0)$. In the case of $I(0)$ by dividing with the value for the primary particles, one obtains a normalized zero-angle intensity, $I(0)_n = I(0)/I(0)_{t=0}$. Within the limits of the Rayleigh–Debye–Gans (RDG) theory (rigorously valid within the following constraints $|m-1| \leq 1$ and $(4\pi R_p/\lambda)|m-1| \leq 1$, where R_p is the radius of the primary particle and m is the relative refractive index), $I(0)$ scales with the second power of the scatterer mass and constitutes a second-order moment of the CMD.[71–74] Outside of these limits, that is, for primary particles of a size comparable to or larger than the laser wavelength,[75–78] or in the case of very dense aggregates, where multiple light scattering within the aggregate is present,[75,77,79] the intensity of the forward scattered light will scale with the mass of the scatterer to a power smaller than two. Accordingly, $I(0)$ will not anymore correspond to the second-order moment of the CMD. To account for these deviations, the following generalized relation is used to relate $I(0)$ to the CMD[69,78]

$$I(0) \propto \sum_i N_i i^{2-c}, \tag{12}$$

where N_i is the concentration of aggregates with dimensionless mass i. The correction factor $c = f(R_p, d_f) \geq 0$ is a complicated function of the primary particle size and the aggregate structure[77] that will be determined experimentally through a scaling approach, where by plotting $I(0)$ vs. $\langle R_g \rangle$, one should obtain a power-law scaling with a slope equal to $d_f(1-c)$.[69]

If the primary particle diameter is within the limits of the RDG theory, and the obtained aggregates are large enough to exhibit a well-developed fractal scaling, the mass fractal dimension of the aggregates, d_f, is an additional quantity, which can be obtained from the slope of the power-law region of the log–log plot of $S(q)$ vs. q. However, outside of these limits, that is, for systems such as those studied in this work, with primary particle diameters comparable to or larger than the laser wavelength,[75,76] with dense aggregates, where multiple light scattering within the aggregates occurs,[75,78,79] with small relative aggregate sizes,[80] or with a certain polydispersity of the CMD,[81] the slope of the power-law region of the log–log plot of $S(q)$ vs. q cannot be directly interpreted as d_f. Therefore, we will denote this slope as the scaling exponent, SE, which is not necessarily equal to d_f. Because of these reasons, the aggregate structure was independently characterized by using image analysis of two-dimensional images of aggregates, taken from samples withdrawn for off-line measurements at various operating conditions. In this way, the structure of aggregates can be

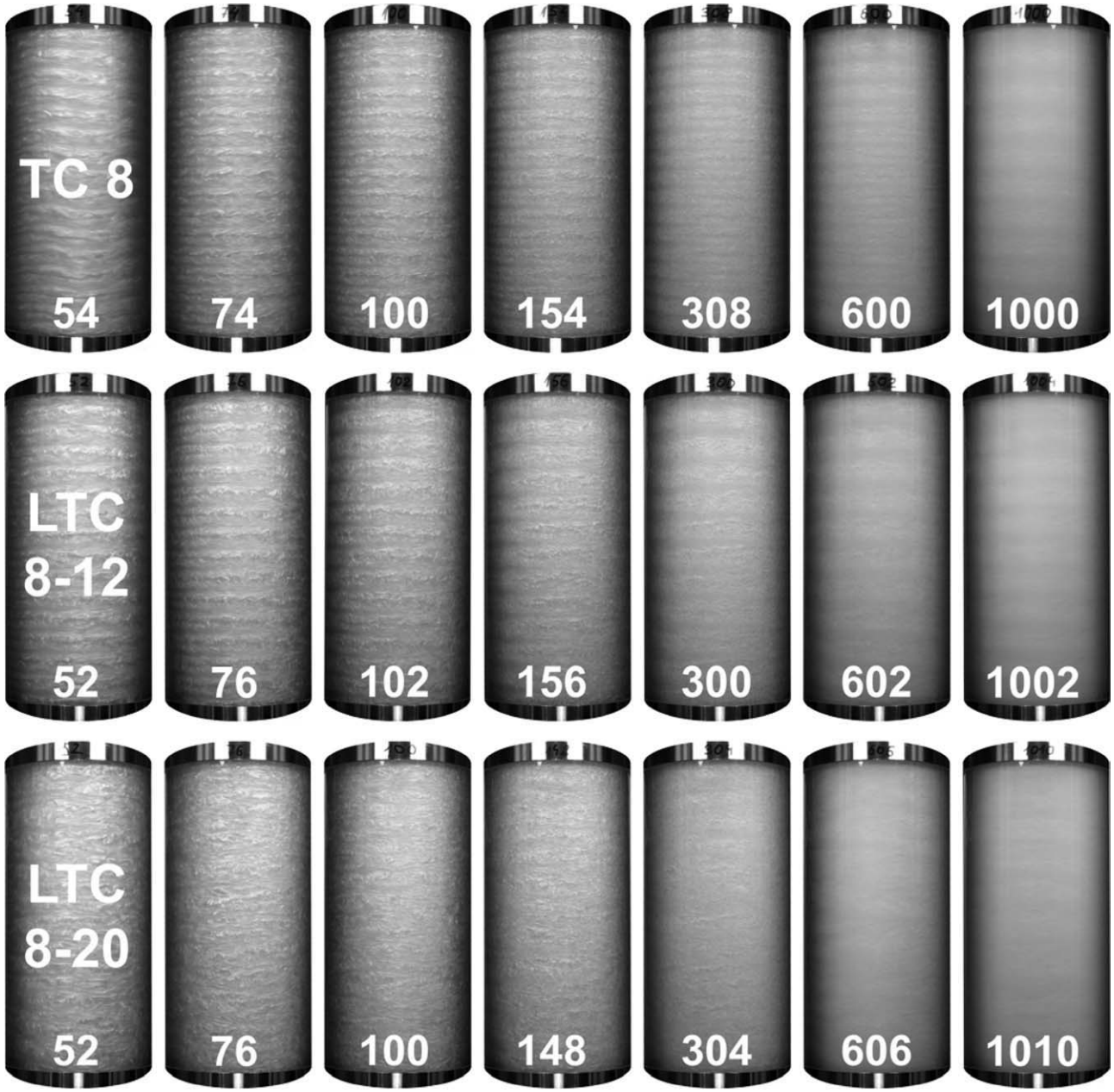

Figure 3. Flow field visualization for the TC-type devices obtained with rheoscopic fluid.

characterized by the perimeter fractal dimension, d_{pf}, obtained from the scaling of the projected surface area, A, vs. the perimeter, P, of the binary images of aggregates,[5,38,46,82]

$$A \propto P^{2/d_{pf}}. \tag{13}$$

Subsequently, the perimeter fractal dimension can be used to evaluate the mass fractal dimension using correlations as presented by Lee and Kramer[83] or by Ehrl et al.[84] As it was shown by Ehrl et al.,[84] this is a very robust method to evaluate the structure of compact aggregates. Detailed description of the experimental methodology, the used measurement techniques, and measurement data analysis can be found in our previous work.[46,68,69]

Results and Discussion

Flow field characterization

Pictures that were obtained from TC-type devices at various stirring speeds using the rheoscopic fluid are shown in Figure 3. It can be clearly seen that for the lowest rpm, for which $Re_{cyl,max}/Re_{cri,max} = 23$, the ordered wavy vortex structure is observed for the TC 8, which is in agreement with literature.[50] When the stirring speed is increased to 74 rpm (corresponding $Re_{cyl,max}/Re_{cri,max} = 31$), turbulent

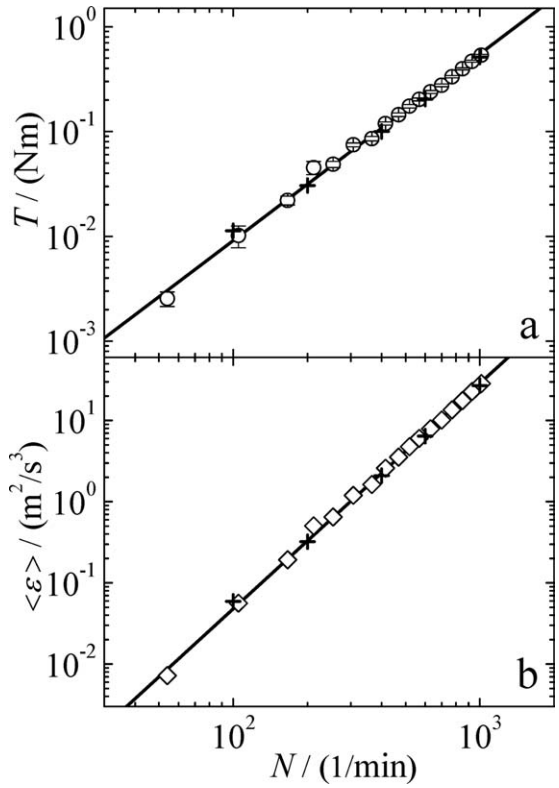

Figure 4. Dependence of (a) torque, *T*, and (b) volume average energy dissipation rate, $\langle\varepsilon\rangle$, on the rotation speed, *N*, for the LTC 8–20.

(○) measured *T* and ◇ $\langle\varepsilon\rangle$ calculated with Eq. 5 using the dimensions of the LTC 8–20 device specified in Table 1; (+)*T* and $\langle\varepsilon\rangle$ obtained from CFD; the solid line represents a power-law fit of the measured values. For the torque measurement, the experimental variations are indicated by error bars.

Taylor vortices are observed in the annular gap of the TC. These stay clearly distinguishable up to a stirring speed of 308 rpm ($Re_{cyl,max}/Re_{cri,max} = 130$). For a further increase above 308 rpm, only slight traces of tangential structure due to vortices are visible, indicating that at these conditions turbulence is well developed. Further, it can be seen that by increasing the maximum gap width at fixed rpm, the ordered structures disappear in favor of more disordered turbulent structures. Namely, for both LTC-type devices, even for the lowest rpm no wavy vortex structure is observable ($Re_{cyl,max}/Re_{cri,max}$ equals 37 and 67 for LTC 8–12 and LTC 8–20, respectively), which is in agreement with the smaller values of $Re_{cri,max}$ as determined earlier. In addition, for increasing stirring speed inside the LTC 8–12, the traces of the secondary flow structure disappear at a smaller stirring speed than in the TC 8, already above 156 rpm ($Re_{cyl,max}/Re_{cri,max} = 112$) the tangential structure due to turbulent Taylor vortices vanishes. For the LTC 8–20, even at the lowest stirring speed no clear tangential structure due to turbulent Taylor vortices is visible. Already at 52 rpm ($Re_{cyl,max}/Re_{cri,max} = 189$), the flow exhibits an irregular structure with increasing disorder for increasing stirring speed. It is noted that because of the shutter speed automatics of the used digital camera the pictures for 1000 rpm are slightly smeared out. In conclusion, the flow field visualization shows that in the case of a changing gap width, the flow pattern is determined by the maximum gap width, and for the conditions applied in the aggregation experiments inside the TC-type devices, the flow passed already the transition region and turbulence is already well developed. Therefore, no reduction of intra- and intervortex mixing due to Taylor vortices is present as reported by Desmet et al.[85] and Snyder.[86] This leads to the conclusion that a nonconstant gap width in azimuthal direction results in destabilizing of the Taylor vortices typical of TC devices.

An example of the relations between *T*, $\langle\tau\rangle$, and *N* that were obtained by torque measurement for the various stirring devices is shown in Figure 4 (LTC 8–20). In both cases, a power-law relation has been observed for larger *N* values. Moreover, good agreement between calculated and experimental values for the net torque was obtained. Similar relations for TC 8 and LTC 8–12 are shown in Supporting Information Figures SM 1 and SM 2, respectively.

To characterize the flow field heterogeneity in all units used in this work, values of the hydrodynamic stresses originating from the mean flow, τ_L, from pressure differences, τ_{IS}, and from velocity fluctuation, τ_{VS}, were evaluated using CFD. It was found that τ_{VS} is dominant in all devices used in this study. This is shown in a contour plot of τ_L, τ_{IS}, and τ_{VS} for ST in Supporting Information Figure SM 7 and for normalized distributions of the three stresses for all devices in Supporting Information Figure SM 8. A comparison of the distribution of the local hydrodynamic stress due to velocity fluctuation evaluated from CFD simulations normalized by the experimentally obtained average stress, $\tau_n = \tau_{VS}/\langle\tau\rangle_{exp}$, for all tested stirring devices is presented in Figure 5. It can be seen that the ST exhibits the broadest τ_{VS}-distribution among the compared devices, covering three orders of magnitude. This is due to the presence of two distinct flow field regions, one close to the impeller exhibiting very large τ_{VS}-values, and the other at the top of the vessel far from the impeller with very low τ_{VS}-values. For the TC 8, the τ_{VS}-distribution is narrower compared with the ST, covering two orders of magnitude. By further deformation of the inner cylinder as shown in Figure 1 for LTC 8–12 and LTC 8–20, the τ_{VS}-distribution narrows even more, covering

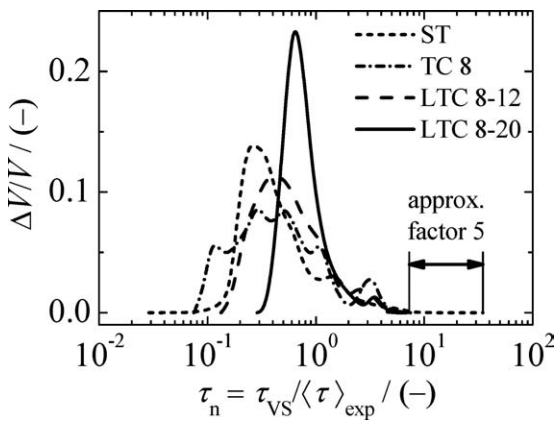

Figure 5. Distributions of the normalized stress, $\tau_n = \tau_{VS}/\langle\tau\rangle_{exp}$, for the four different devices used.

The ratio of the maximum normalized stresses for the ST and the TC-type devices takes a value of ~5.

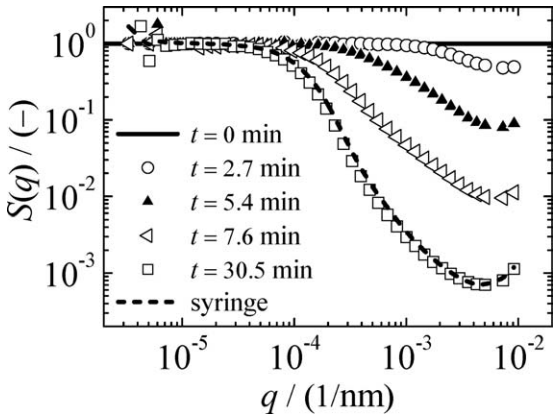

Figure 6. Structure factors measured at various times for a solid volume fraction equal to 2×10^{-5} and a stirring speed of 250 rpm in the TC 8 device.

The symbols correspond to the structure factors measured at various times using on-line loop measurement, and the dashed line represents an example of the structure factor from an off-line sample obtained at $t = 30.5$ min.

1.8 and 1.4 orders of magnitude, respectively. This difference between ST- and TC-type devices is a result of the distinct mechanisms of the fluid motion induced by the impeller. Whereas in the ST fluid motion (momentum) is generated by the impeller blades pushing (pumping) the liquid, in the TC-type devices the momentum is transferred from the rotating inner cylinder to the liquid purely via viscous interactions.

According to the results obtained from CFD analysis of the flow field in ST- and TC-type devices, when discussing the effect of the hydrodynamic stress on the process of aggregation and breakage, the values of the hydrodynamic stress originating from the velocity fluctuation, τ_{VS}, or its volume average values measured experimentally, $\langle \tau_{VS} \rangle_{exp} = \mu \sqrt{\langle \varepsilon \rangle / \nu}$, will be used. For simplicity for the latter one, the symbol $\langle \tau \rangle_{exp}$ will be used.

Example of an aggregation experiment

Before discussing the individual observations and phenomena related to the effect of the flow field heterogeneity on aggregation in the various devices used in this work, let us start with a typical aggregation experiment. Under steady stirring, after destabilization, the particles in the dispersion start to aggregate and form large clusters. In the initial phase, this process is self-accelerating, and the kinetics is exponential. After reaching a certain size, aggregate breakup sets in and the growth rate decays until a steady-state aggregate size is reached. The steady state depends on the stirring intensity, the solid volume fraction of the system, and the aggregates strength, which is determined by the interactions between the primary particles and the aggregate structure. An example of the measured structure factors obtained by on-line small-angle static light scattering at various process times using the TC 8 device is presented in Figure 6. As can be seen, with time increasing the position where $S(q)$ starts to bend (Guinier region) down from its plateau value toward the power-law region shifts to lower q-values, which is equivalent to an increase in aggregate size. These data (symbols) are obtained using the on-line loop technique as described earlier. Additionally, to verify that the flow rate in the measurement loop is selected properly and, therefore, does not affect the aggregate size, the steady-state structure factors obtained at $t = 30.5$ min both by on-line measurement (open squares) and off-line sampling (dashed line) are compared in Figure 6. As can be seen, the corresponding $S(q)$ shows good agreement. The time evolution of two integral quantities of the CMD, $\langle R_g \rangle$ and $I(0)$, for the TC 8 device, obtained from the analysis of structure factors as presented in Figure 6, is plotted in Figure 7. For comparison to the on-line results, also the steady-state values of $\langle R_g \rangle$ and $I(0)$ obtained from off-line samples withdrawn with syringes at various heights of the device are presented in Figure 7. It can be seen that both techniques (off-line and on-line) agree well, and no difference exists between the different sampling ports along the cylinder. This proves that for the applied process conditions (pump speed and low solid volume fraction), the on-line measurement technique is applicable, and that the sampling location has no influence on the measurement results at steady state. Such a validation of the measurement procedure is essential, as in processes involving aggregation

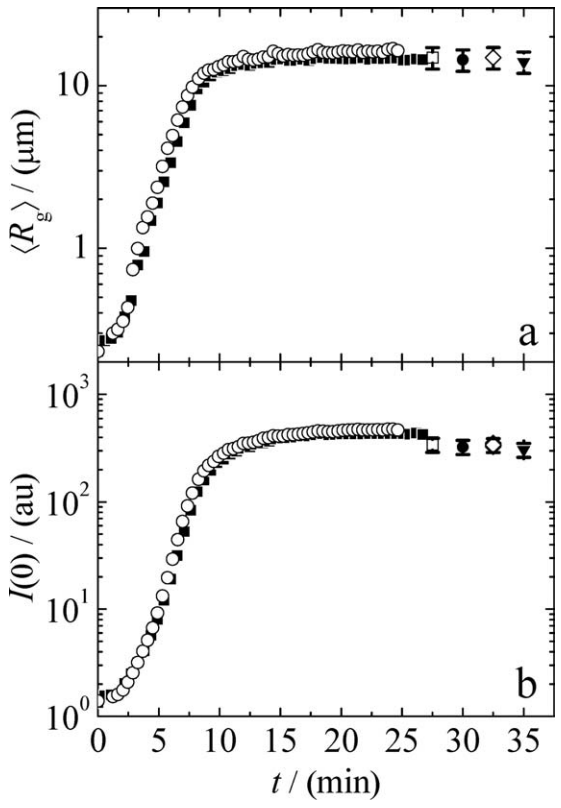

Figure 7. Typical example of the time evolution of (a) the rms radius of gyration, $\langle R_g \rangle$, and (b) the absolute zero-angle intensity, $I(0)$ (in arbitrary units, au), measured for a solid volume fraction equal to 2×10^{-5} and a stirring speed of 250 rpm in the TC 8 device.

(■○) loop measurement, and validation measurements (syringe) for the sampling ports (□) c, (●) d, (◇) e, and (▼) b (see Figure 2).

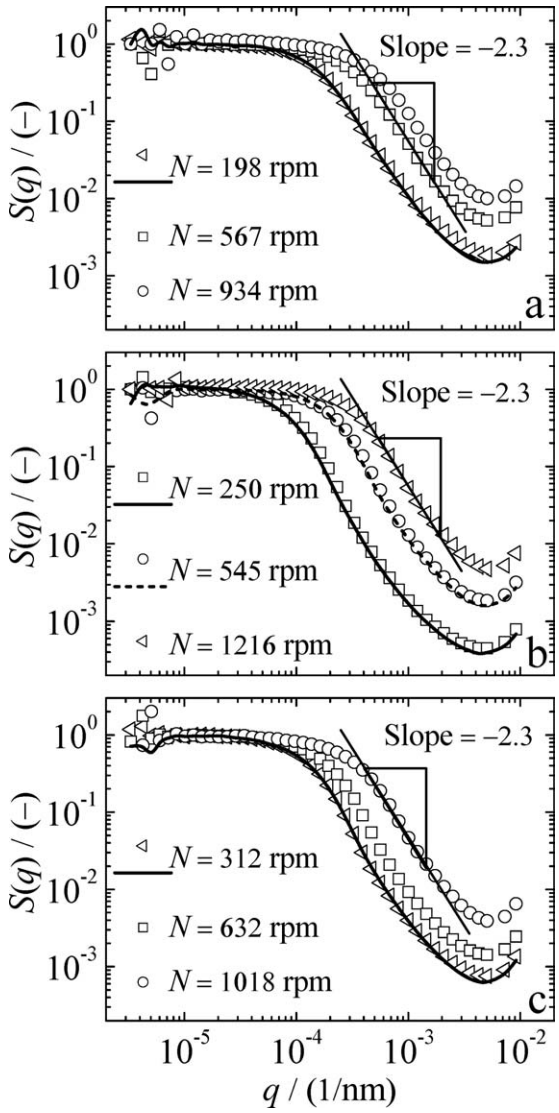

Figure 8. Comparison of steady-state *S*(*q*) measured for various rotation speeds using (a) ST, (b) TC 8, and (c) LTC 8–20.

All curves presented here were obtained in single experiments with (a) ST N = 198-384-567-934-198rpm, (b) TC 8 N = 250-586-1216-586-250 rpm, and (c) LTC 8–20 N = 312-632-1018-312 rpm, respectively, measured for a solid volume fraction equal to 2×10^{-5}. The lines correspond to steady-state $S(q)$ measured after readjusting the stirring speed the value used at the beginning of the experiment.

and breakage mechanisms, depending on the applied process conditions and measurement technique, one or both of the two mechanisms can easily falsify the measurement results. A validation of the on-line loop measurement technique for the ST coagulator that is used in this work was presented by Moussa et al.[68]

Reversibility of steady-state cluster mass distributions

As in our previous work,[46,68–70] where we observed reversibility of the steady-state values for both integral quantities of the CMD, $\langle R_g \rangle$ and $I(0)$, using polystyrene latexes with various primary particle sizes, we investigated the steady-state reversibility also for the latex system used in this work. To do so, aggregation experiments are run at a certain stirring speed until steady state is reached, then the stirring speed is changed stepwise, each time awaiting new steady state. Finally, the stirring speed is selected such to be again equal to that used at the beginning of the experiment. In this way, during one experiment, several steady-state values are collected, and the reversibility of the process is tested. An example of the resulting structure factors, $S(q)$, at the various stirring speeds measured in ST, TC 8, and LTC 8–20 is shown in Figure 8. The corresponding graph for LTC 8–12 is shown in Supporting Information Figure SM 3. It can be seen that for higher rpm the bending part (Guinier region) moves to higher q-values, indicating smaller aggregates, whereas the slope of the power-law scaling stays constant with a slope equal to −2.3. The structure factors are history independent and depend only on the current process conditions proving full steady-state reversibility of the investigated latex system for all studied devices. Corresponding time evolution of $\langle R_g \rangle$ and $I(0)$ for the TC 8 device obtained from the analysis of the structure factors measured on-line

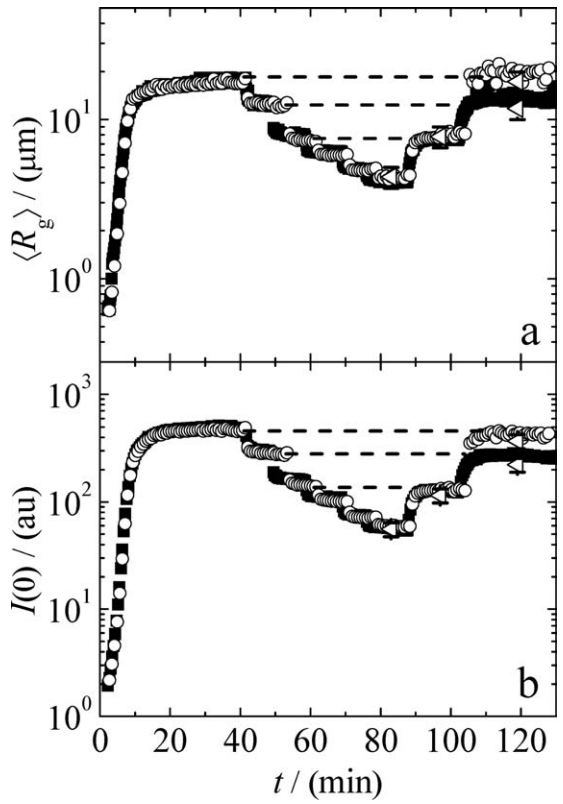

Figure 9. Examples of the time evolution of (a) the rms radius of gyration, $\langle R_g \rangle$, and (b) the absolute zero-angle intensity, $I(0)$ (in arbitrary units, au), during step changes in stirring speed, for the TC 8 device, measured for a solid volume fraction equal to 2×10^{-5}.

The stirring speed was changed in the following manner: (■) N = 250-362-544-718-988-1216-546-362rpm; (○) N = 250-362-586-754-1012-1202-586-250rpm; (■○) loop measurement, (◁) validation measurements (syringe).

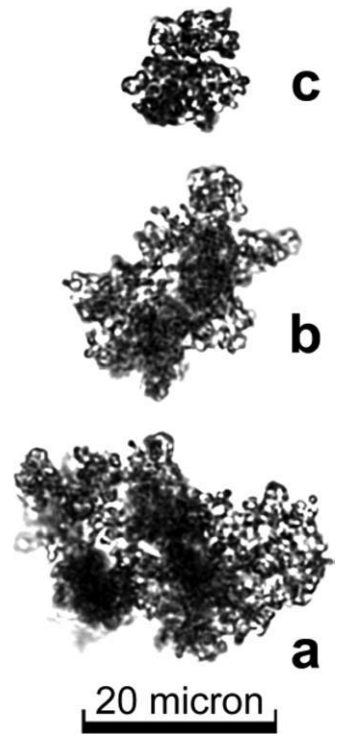

Figure 10. (a–c) Images of aggregates obtained by confocal laser scanning microscopy from samples taken at steady state for various values of the stirring speed, (a) 250, (b) 506, and (c) 1018 rpm, and a solid volume fraction equal to 2×10^{-5} produced in the TC 8 device.

by light scattering is presented in Figure 9. As already seen from $S(q)$, full steady-state reversibility of the system is also observed for both integral quantities of the CMD. This indicates that the structure of the aggregates obtained at steady state should also be independent of the shear rate history. Corresponding graphs for the LTC 8–12, LTC 8–20, and ST are shown in Supporting Information Figures SM 4–6, respectively.

Aggregate structure and shape obtained from image analysis

Because of the large size of primary particles with respect to the laser wavelength[75–77] and the expected compactness of aggregates produced under turbulent conditions,[75,77,79] the mass fractal dimension cannot be deduced directly from the power-law scaling of $S(q)$. Hence, the aggregate structure was determined by analyzing images of aggregates obtained via off-line sampling.[84] Examples of confocal laser scanning microscopy images of aggregates are presented in Figure 10. Note that similar structure factors obtained by on-line and off-line scattering measurements (see Figures 6,7, and 9) demonstrate that the sampling procedure affects neither the size nor the structure of the aggregates. The resulting relation between the area and perimeter of the two-dimensional projections of aggregates produced in the TC 8 at three different stirring speeds is shown in Figure 11. It is worth noting that to obtain statistically relevant data for each operating condition, at least 70 aggregate images were evaluated with respect to 2D properties, that is, perimeter, area, and aspect ratio. The slope of the obtained power-law scaling is equal to $2/d_{pf} = 1.7$, which applying the relation between d_{pf} and d_f developed by Lee and Kramer[83] and by Ehrl et al.[84] results in $d_f = 2.65 \pm 0.2$. This serves as further support that the reversibility of the steady state as discussed earlier is connected with the aggregate structure being independent of the operating conditions. Moreover, comparing this value of d_f with those obtained in ST using various primary particle sizes ($d_f = 2.62 \pm 0.18$ as reported by Soos et al.[46] and $d_f = 2.62 \pm 0.18$ as reported by Ehrl et al.[69]) evidences that under turbulent conditions, the aggregate structure for the investigated latex systems (surfactant-free polystyrene latexes with relatively large surface charge density) is compact and independent of the flow field heterogeneity.

Another information that one can obtain from the image analysis is the aggregates shape, characterized here by their aspect ratio, that is, the ratio of the major and minor axes of the best fitted ellipse. In Figure 12 are plotted the distributions of the aggregates aspect ratio obtained at various stirring speeds in the case of the TC 8 device. It can be seen that the shape of the distribution does not change significantly with values ranging from 1 to 3 and a peak value around 1.3. These results are similar to the findings in ST device,[46,69] supporting a general shape of the aggregates produced under turbulent conditions independent of the flow field heterogeneity.

Scaling of steady-state $\langle R_g \rangle$ and I(0) with experimental average stress and aggregate strength

The steady-state aggregate size is a result of a dynamic equilibrium between aggregation and breakage. As the rate constants of both aggregation[26–28] and breakage[29] are not linearly dependent on shear rate, for devices exhibiting significantly different distributions of the shear rate and, therefore, different τ_{VS}-distributions, one should expect a

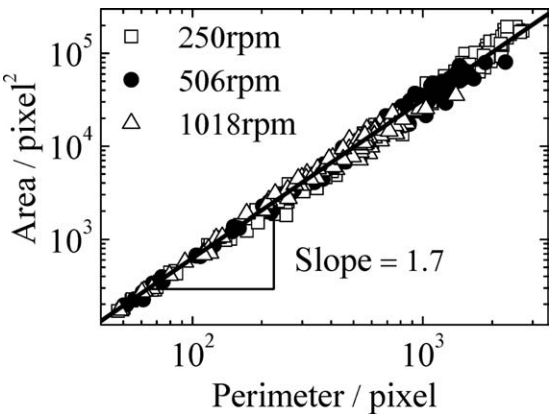

Figure 11. Relationship between area and perimeter obtained by image analysis for a solid volume fraction equal to 2×10^{-5} and various values of the stirring speed produced in the TC 8 device.

To obtain statistically reliable data, at least 70 aggregates were analyzed for each stirring speed.

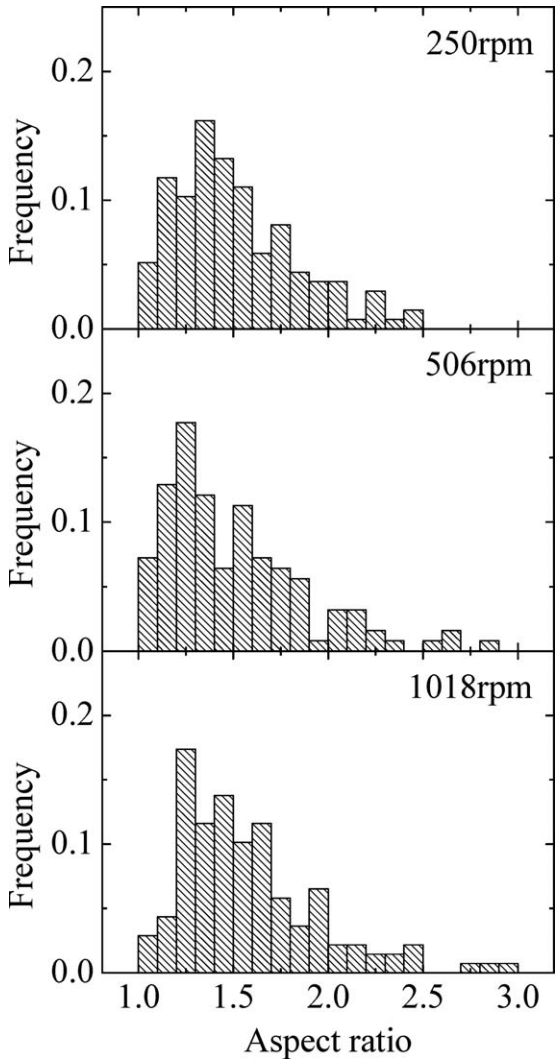

Figure 12. Comparison of the distributions of aggregates aspect ratio at steady state obtained from confocal laser scanning microscopy images, various values of the stirring speed and a solid volume fraction equal to 2 × 10^{-5} produced in the TC 8 device.

difference in the obtained steady-state values of $\langle R_g \rangle$ and $I(0)$ (or $I(0)_n$). This effect of the flow field heterogeneity becomes apparent in Figure 13, where steady-state values of $\langle R_g \rangle$ and $I(0)_n$ are plotted as functions of experimentally measured average hydrodynamic stress originating from velocity fluctuation, $\langle \tau \rangle_{exp} = \mu \sqrt{\langle \varepsilon \rangle / \nu}$, both for the TC-type devices and the ST. It can be seen that the absolute values of $\langle R_g \rangle$ and $I(0)_n$ obtained in ST are shifted down dramatically compared with TC-type devices, while the slope of the scaling for both quantities is preserved, with values equal to -0.5 for $\langle R_g \rangle$ and -0.7 for $I(0)$. It is worth mentioning that for the observed d_f the value of -0.5 in the case of $\langle R_g \rangle$ is in agreement with theoretical consideration of Zaccone et al.[87] on the breakup of dense colloidal aggregates caused by hydrodynamic stresses.

Now, we want to recall the experimental observations of significantly smaller absolute values of $\langle R_g \rangle$ and $I(0)_n$ obtained in ST compared with the TC-type devices. In particular, for the same aggregates size (Figure 13a), the value of the experimental average hydrodynamic stress is approximately five times larger inside TC-type devices than inside ST. Comparing the distribution of normalized τ_{VS} in all devices from Figure 5, this can be attributed to the fact that also the maximum hydrodynamic stress inside ST is approximately five times larger than that inside the TC-type devices. This trend is in agreement with the findings of Coufort et al.[16] obtained for bentonite in a jar and a TC-reactor, where for the same $\langle \varepsilon \rangle$ aggregates of smaller sizes were obtained inside a ST compared with a TC device. The measured trend is further supported by the work of Ducoste et al.[37] who found that if one keeps a constant $\langle G \rangle$ for different tank sizes the turbulent intensity in the discharge zone increases as the tank size increases, and it follows that aggregate breakup increases, leading to smaller sizes of aggregates.

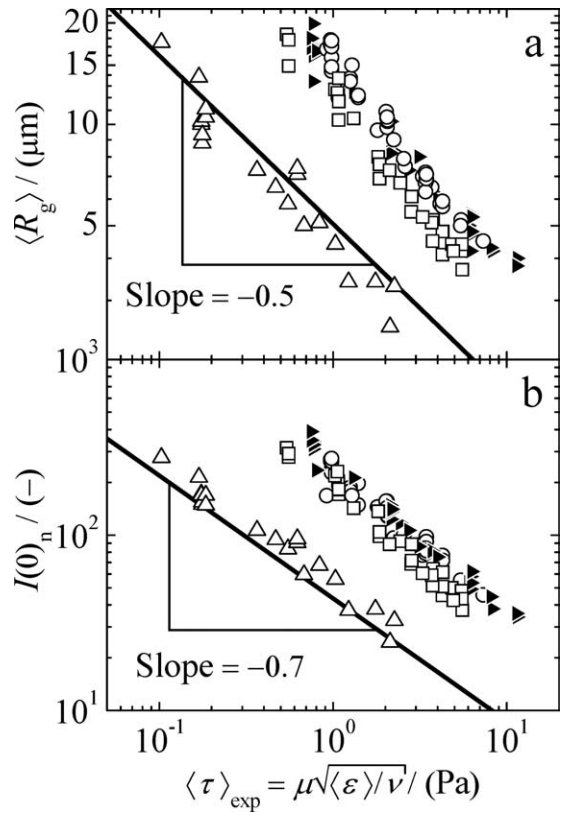

Figure 13. Scaling of the steady-state (a) rms radius of gyration, $\langle R_g \rangle$, and (b) normalized zero-angle intensity, $I(0)_n = I(0)/I(0)_{t=0}$, as a function of the experimentally obtained average hydrodynamic stress, $\langle \tau \rangle_{exp} = \mu \sqrt{\langle \varepsilon \rangle / \nu}$, measured in (▶) TC 8, (○) LTC 8–12, (□) LTC 8–20, and (△) ST, for a solid volume fraction equal to 2 × 10^{-5}.

The solid line in inlet (a) corresponds to the minimum Kolmogorov microscale within ST.

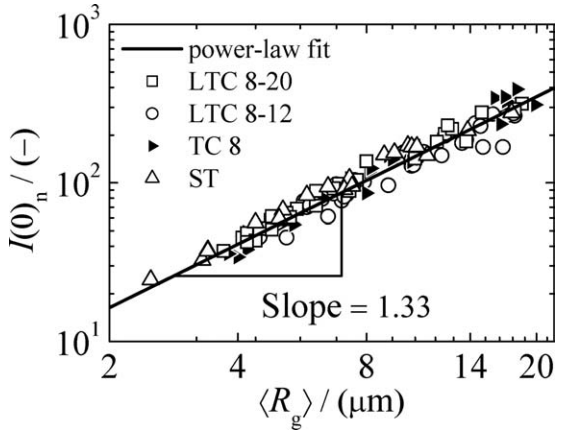

Figure 14. Scaling of the steady-state values of the normalized zero-angle intensity, $I(0)_n = I(0)/I(0)_{t=0}$, as a function of the rms radius of gyration, $I(0)$, for different coagulations units and a solid volume fraction equal to 2×10^{-5}.

On the other hand, the fact that similar steady-state values of $\langle R_g \rangle$ and $I(0)_n$ are observed for the three different TC-type devices indicates that the maximum hydrodynamic stresses of those devices take similar values, which is in agreement with the τ_{VS}-distributions presented in Figure 5. This can be attributed to the fact that their impeller geometry is quite similar, cylindrical or lobed cross section with smooth surfaces and the same minimum gap width, leading to similar maximum hydrodynamic stresses inside these devices. These observations are supported by the findings of Spicer et al.[38] and Simmons et al.[43] In the work of Spicer et al.,[38] the effect of impeller type (at constant $\langle G \rangle$) on the steady-state aggregate size was studied. As the impellers conformed in the general features, that is, the impellers were all bladed with equal diameters, no significant differences in the aggregation behavior with respect to the used impeller were observed. Accordingly, by measuring the local rate of energy dissipation within ST devices for bladed impellers of various shapes using particle image velocimetry, Simmons et al.[43] found comparable maximum values of the energy dissipation rate for impellers of the same diameter.

In conclusion, for the system under investigation (surfactant-free polystyrene latex with relatively large surface charge density), a comparison of the relevant hydrodynamic stresses showed that for the observed aggregate sizes, aggregate breakup is determined by viscous stresses. It is observed that the CMD is affected by the heterogeneity of the flow field. However, identical scaling behavior of $\langle R_g \rangle$ and $I(0)_n$ with the hydrodynamic stress for all devices has been obtained, which likewise is in agreement with a conception of aggregate breakup occurring in the viscous subrange, whose characteristic length scale η_K, according to the Richardson[88] and Kolmogorov[89,90] energy cascade, scales independently from device geometry with $\sqrt[4]{\nu^3/\varepsilon}$. Furthermore, when the maximum value of the hydrodynamic stress or the broadness of its distribution determines system performance, for example, fermentation of mammalian cells, presented results can be used to optimize operating conditions of existing bioreactors or they can be used during design of novel fermentation systems.[42]

Light scattering properties of formed clusters

It is known that for systems such as that investigated in this work, multiple scattering within the aggregates is present,[69,77,78] leading to a scaling of $I(0)$ (or $I(0)_n$) with $\langle R_g \rangle$ not following the fractal scaling law, $I(0) \propto \langle R_g \rangle^{d_f}$. However, as it was shown by Ehrl et al.,[69] plotting $I(0)$ vs. $\langle R_g \rangle$ provides a way to experimentally determine the correction factor, c, to the RDG theory due to multiple light scattering within the aggregates once the fractal dimension is known ($I(0) \propto \langle R_g \rangle^{d_f(1-c)}$). Such a plot of $I(0)_n$ vs. $\langle R_g \rangle$ is shown in Figure 14, where the slope of the power-law fit equals 1.33, which is in the range of values reported by Ehrl et al.[69] (1.50 and 1.24 for dense clusters made of 420 and 810 nm sized primary particles, respectively), as well as in agreement with the theoretical prediction of light scattering behavior of dense clusters of colloidal nanoparticles by Lattuada and Ehrl.[77]

As $I(0)_n$ and $\langle R_g \rangle$ represent two distinct moment ratios of the CMD, their ratio provides a measure of the polydispersity of the aggregate populations. This entails that for distributions of significant different polydispersity, the curves of $I(0)$ vs. $\langle R_g \rangle$ should not collapse onto a unique curve. However, in Figure 14, it can be seen that not only the scaling of $I(0)_n$ vs. $\langle R_g \rangle$ for all devices follows the same power-law but also they have the same intercept as the measurement points scatter all around the same line. This is an indication that the polydispersity of the aggregate mass distributions is similar for the four devices investigated.

Conclusions

In this work, the effect of the flow field heterogeneity on steady-state aggregate size and structure was studied in a systematic manner to clarify the contradictory results presented in the literature.[11,12,16,37,39] For this purpose, aggregation experiments with fully destabilized polystyrene particles, 600 nm in diameter, were performed inside various stirring devices whose flow field, in terms of the distribution of the local hydrodynamic stress, differs significantly. One classical TC device (TC 8), two TC-type devices with lobed inner cylinders (LTC 8–12 and LTC 8–20), and a ST, equipped with Rushton impeller, were compared. The aggregate size, in terms of root-mean-square radius of gyration, $\langle R_g \rangle$, and (normalized) zero-angle intensity of scattered light, $I(0)$ ($I(0)_n$), were determined from structure factors obtained from on-line small-angle static light scattering measurements. Because of the uncertainties in the evaluation of the aggregate structure from light scattering data, the aggregate structure was determined by image analysis of two-dimensional projections of aggregates sampled off-line. Experiments applying stepwise changes of the stirring speed showed full reversibility of both the steady-state structure factors, and therefore $\langle R_g \rangle$ and $I(0)$ ($I(0)_n$), as well as the aggregate structure obtained from image analysis. It was found that for the same experimental average hydrodynamic stress obtained from torque measurements, $\langle \tau \rangle_{exp} = \mu \sqrt{\langle \varepsilon \rangle / \nu}$, the aggregates grow up to sizes, which are approximately three to four

times larger inside the TC-type devices compared with the ST, whereas no significant difference for the three studied TC-type devices was observed. This observation is explained by a larger value of the maximum hydrodynamic stress inside ST, evaluated by CFD, which is approximately five times larger compared with that obtained for TC-type devices. In contrast to this difference, the slopes of the power-law scaling of both $\langle R_g \rangle$ and $I(0)_n$ plotted as a function of $\langle \tau \rangle_{exp}$ for both types of devices are preserved with values equal to -0.5 in the case of $\langle R_g \rangle$ and -0.7 for $I(0)$. In addition, the aggregate structure with $d_f = 2.65 \pm 0.2$ and the aggregate shape, characterized by their aspect ratios with values ranging from 1 to 3 with a maximum around 1.3, are very similar to those measured in our previous work for ST.

Moreover, a plot of $I(0)_n$ vs. $\langle R_g \rangle$ provided two more conclusions. First, it was found that also the polydispersity of the aggregate populations is independent of the applied device. Second, this plot allows for the experimental estimation of the effect of multiple light scattering within the aggregates, because of large primary particle size and dense structure. A correction factor, c, for a modified fractal scaling approach, $I(0)_n \propto \langle R_g \rangle^{d_f(1-c)}$, with a value equal to 1.33 was obtained, which is in good agreement with the literature data.[77,84] By combining all this information, we can conclude that for the investigated colloidal system (surfactant-free polystyrene latex with relatively large surface charge density) aggregated under turbulent conditions, the structure and shape of aggregates are independent of the type of device, and further the CMD is indeed affected by the heterogeneity of the flow field, but identical scaling behavior of $\langle R_g \rangle$ and $I(0)_n$ with the hydrodynamic stress for all devices has been obtained. This is in agreement with the conception of aggregate breakup occurring in the viscous subrange, where the characteristic length scale, η_K, scales independently from device geometry with $\sqrt[4]{\nu^3/\varepsilon}$.

The following practical conclusions can be drawn for reversible systems under dilute and turbulent conditions: (1) the maximum aggregate size is determined by the maximum hydrodynamic stress present in the system, that is, to obtain aggregates of same size and structure, TC-type devices can be operated at much higher energy input compared with ST; (2) the scaling of aggregate size with power input is independent of the stirring device, that is, if the ratio of power input necessary to obtain a certain size ratio is known for one device it can be directly transformed to another; and (3) the aggregate structure is independent of the stirring device and intensity.

Acknowledgments

The authors thank Dr. Matthäus Ulrich Bäbler for useful discussions and helpful suggestions. This work was financially supported by the Swiss National Science Foundation (Grant No. 200020-126487/1).

Notation

Roman letters

A = area of aggregates from microscopy images, pixel^2
c = correction factor for scaling of $I(0)$ with i, which is a function of d_p and d_f
d_{agg} = aggregate diameter, m
d_f = mass fractal dimension
d_{gap} = gap width, distance between inner and outer cylinder, m
d_{imp} = impeller diameter, m
d_{pf} = perimeter fractal dimension, $A \propto P^{2/d_{pf}}$
d_{tank} = tank diameter, m
$\langle G \rangle$ = volume average shear rate, $\langle G \rangle = \sqrt{\langle \varepsilon \rangle / \nu}$, s^{-1}
i = dimensionless aggregate mass
$I(0)$ = zero-angle intensity of scattered light, au
$I(q)$ = intensity of scattered light at q, au
$I(0)_n$ = normalized zero-angle intensity of scattered light, $I(0)_n = I(0)/I(0)_{t=0}$
m = relative refractive index
n = refractive index
N = rotations of inner cylinder per minute, min^{-1}
N_i = absolute number of aggregates with normalized mass i
P = perimeter of aggregates from microscopy images, pixel
$P(q)$ = form factor of primary particles
q = scattering wave vector amplitude, as defined in Eq. 11, nm^{-1}
r_i, r_o = radius of inner and outer cylinder, m
Re_{cri} = critical Reynolds number, $Re_{cri} = (Ta_{cri}\nu/(\omega_i d_{gap}^2))$
Re_{cyl} = inner cylinder Reynolds number, as defined in Eq. 1
Re_{imp} = impeller Reynolds number, as defined in Eq. 4
R_g = radius of gyration, μm
$\langle R_g \rangle$ = root-mean-square radius of gyration, $\langle R_g \rangle = \sqrt{\langle R_g^2 \rangle}$, μm
R_p = primary particle radius, nm
SE = scaling exponent of the power-law region of the intensity curve
$S(q)$ = structure factor as a result of primary particle arrangement
t = time, s
T = torque, Nm
Ta_{cri} = critical Taylor number, as defined in Eq. 3
Ta_{cyl} = inner cylinder Taylor number, as defined in Eq. 2
V = reactor volume, m^3

Greek letters

α_L = maximum positive eigenvalue of the rate of strain tensor under laminar conditions, s^{-1}
ε, $\langle \varepsilon \rangle$' = local and volume average energy dissipation rate, m^2 s^{-3}
η_K = Kolmogorov length scale, as defined in Eq. 7, m
θ = scattering angle, rad
λ = laser wave length, m
μ = dynamic viscosity, in this work a value of 10^{-3} Pa s (water at 25°C) was used, Pa s
ν = kinematic viscosity, in this work a value of 10^{-6} m^2 s^{-1} (water at 25°C) was used, m^2 s^{-1}
ρ = density of water, in this work a value of 10^3 kg m^{-3} (water at 25°C) was used, kg m^{-3}
$\langle \tau \rangle_{exp}$ = experimental average hydrodynamic stress, $\langle \tau \rangle_{exp} = \mu\sqrt{\langle \varepsilon \rangle / \nu}$, Pa
τ_L, τ_{IS}, τ_{VS} = local hydrodynamic stress due to mean flow, pressure fluctuations, and viscous forces, Pa
τ_n = normalized local hydrodynamic stress under turbulent conditions, $\tau_n = \tau_{VS}/\langle \tau \rangle_{exp}$, Pa
ω_i = angular velocity of inner cylinder, rad

Abbreviations

CMD = cluster mass distribution
LTC = lobed Taylor–Couette
ST = stirred tank
TC = Taylor–Couette
RDG = Rayleigh–Debye–Gans

Literature Cited

1. Letterman RD, Amirtharajah A, O'Melia CR. *Coagulation and flocculation*. In: Letterman RD, editor. *Water Quality and Treatment—A Handbook of Community Water Supplies*, 5th ed. McGraw-Hill, New York, NY, 1999:6.1–6.66.

2. Odian G. *Principles of Polymerization*, 4th ed. Hoboken, NJ: Wiley, 2004.
3. Reich I, Vold RD. Flocculation-deflocculation in agitated suspensions. I. Carbon and ferric oxide in water. *J Phys Chem.* 1959;63:1497–1501.
4. Oles V. Shear-induced aggregation and breakup of polystyrene latex particles. *J Colloid Interface Sci.* 1992;154:351–358.
5. Spicer PT, Pratsinis SE. Shear-induced flocculation: the evolution of floc structure and the shape of the size distribution at steady state. *Water Res.* 1996;30:1049–1056.
6. Kusters KA, Wijers JG, Thoenes D. Aggregation kinetics of small particles in agitated vessels. *Chem Eng Sci.* 1997;52:107–121.
7. Serra T, Colomer J, Casamitjana X. Aggregation and breakage of particles in a shear flow. *J Colloid Interface Sci.* 1997;187:466–473.
8. Flesch JC, Spicer PT, Pratsinis SE. Laminar and turbulent shear-induced flocculation of fractal aggregates. *AIChE J.* 1999;45:1114–1124.
9. Biggs CA, Lant PA. Activated sludge flocculation: on-line determination of floc size and the effect of shear. *Water Res.* 2000;34:2542–2550.
10. Bouyer D, Liné A, Cockx A, Do-Quang Z. Experimental analysis of floc size distribution and hydrodynamics in a jar-test. *Chem Eng Res Des.* 2001;79:1017–1024.
11. Selomulya C, Amal R, Bushell G, Waite TD. Evidence of shear-rate dependence on restructuring and breakup of latex aggregates. *J Colloid Interface Sci.* 2001;236:67–77.
12. Selomulya C, Bushell G, Amal R, Waite TD. Aggregation mechanisms of latex of different particle sizes in a controlled shear environment. *Langmuir.* 2002;18:1974–1984.
13. Wang L, Vigil RD, Fox RO. CFD simulation of shear-induced aggregation and breakage in turbulent Taylor-Couette flow. *J Colloid Interface Sci.* 2005;285:167–178.
14. Waldner MH, Sefcik J, Soos M, Morbidelli M. Initial growth kinetics of aggregates in turbulent coagulator. *Powder Technol.* 2005; 156:226–234.
15. Wang L, Marchisio DL, Vigil RD, Fox RO. CFD simulation of aggregation and breakage processes in laminar Taylor-Couette flow. *J Colloid Interface Sci.* 2005;282:380–396.
16. Coufort C, Bouyer D, Liné A. Flocculation related to local hydrodynamics in a Taylor-Couette reactor and in a jar. *Chem Eng Sci.* 2005;60:2179–2192.
17. Soos M, Wu H, Morbidelli M. A Taylor-Couette unit with lobed inner cylinder cross section. *AIChE J.* 2007;53:1109–1120.
18. Zhou GW, Kresta SM. Impact of tank geometry on the maximum turbulence energy dissipation rate for impellers. *AIChE J.* 1996;42:2476–2490.
19. Sharp KV, Adrian RJ. PIV study of small-scale flow structure around a Rushton turbine. *AIChE J.* 2001;47:766–778.
20. Escudie R, Line A. Experimental analysis of hydrodynamics in a radially agitated tank. *AIChE J.* 2003;49:585–603.
21. Baldi S, Yianneskis M. On the quantification of energy dissipation in the impeller stream of a stirred vessel from fluctuating velocity gradient measurements. *Chem Eng Sci.* 2004;59:2659–2671.
22. Ducci A, Yianneskis M. Direct determination of energy dissipation in stirred vessels with two-point LDA. *AIChE J.* 2005;51:2133–2149.
23. Derksen J, Van den Akker HEA. Large eddy simulations on the flow driven by a Rushton turbine. *AIChE J.* 1999;45:209–221.
24. Delafosse A, Line A, Morchain J, Guiraud P. LES and URANS simulations of hydrodynamics in mixing tank: comparison to PIV experiments. *Chem Eng Res Des.* 2008;86:1322–1330.
25. Murthy BN, Joshi JB. Assessment of standard k-epsilon, RSM and LES turbulence models in a baffled stirred vessel agitated by various impeller designs. *Chem Eng Sci.* 2008;63:5468–5495.
26. van de Ven TGM, Mason SG. Microrheology of colloidal dispersions. VII. Orthokinetic doublet formation of spheres. *Colloid Polym Sci.* 1977;255:468–479.
27. Zeichner GR, Schowalter WR. Use of trajectory analysis to study stability of colloidal dispersion in flow fields. *AIChE J.* 1977; 23:243–254.
28. Bäbler MU. A collision efficiency model for flow induced coagulation of fractal aggregates. *AIChE J.* 2008;54:1748–1760.
29. Bäbler MU, Morbidelli M, Baldyga J. Modeling the breakup of solid aggregates in turbulent flows. *J Fluid Mech.* 2008;612:261–289.
30. Marchisio DL, Soos M, Sefcik J, Morbidelli M. Role of turbulent shear distribution in aggregation and breakage processes. *AIChE J.* 2006;52:158–173.
31. Marchisio DL, Soos M, Sefcik J, Morbidelli M, Barresi AA, Baldi G. Effect of fluid dynamics on particle size distribution in particulate processes. *Chem Eng Technol.* 2006;29:191–199.
32. von Smoluchowski M. Versuch einer mathematischen Theorie der Koagulationskinetik kolloider Lösungen. *Zeitschrift für Phys Chem.* 1917;92:129–168.
33. Alopaeus V, Koskinen J, Keskinen KI. Simulation of the population balances for liquid-liquid systems in a nonideal stirred tank. I. Description and qualitative validation of the model. *Chem Eng Sci.* 1999;54:5887–5899.
34. Alopaeus V, Koskinen J, Keskinen KI, Majander J. Simulation of the population balances for liquid-liquid systems in a nonideal stirred tank. II. Parameter fitting and the use of the multiblock model for dense dispersions. *Chem Eng Sci.* 2002;57:1815–1825.
35. Ducoste JJ. A two-scale PBM for modeling turbulent flocculation in water treatment processes. *Chem Eng Sci.* 2002;57:2157–2168.
36. Kramer TA, Clark MM. Modeling orthokinetic coagulation in spatially varying laminar flow. *J Colloid Interface Sci.* 2000;227:251–261.
37. Ducoste JJ, Clark MM, Weetman RJ. Turbulence in flocculators: effects of tank size and impeller type. *AIChE J.* 1997;43:328–338.
38. Spicer PT, Keller W, Pratsinis SE. The effect of impeller type on floc size and structure during shear-induced flocculation. *J Colloid Interface Sci.* 1996;184:112–122.
39. Serra T, Colomer J, Logan BE. Efficiency of different shear devices on flocculation. *Water Res.* 2008;42:1113–1121.
40. Ochoa JC, Coufort C, Escudie R, Line A, Paul E. Influence of non-uniform distribution of shear stress on aerobic biofilms. *Chem Eng Sci.* 2007;62:3672–3684.
41. Nienow AW. Reactor engineering in large scale animal cell culture. *Cytotechnology.* 2006;50:9–33.
42. Tanzeglock T. A novel lobed taylor-couette bioreactor for the cultivation of shear sensitive cells and tissues. PhD Thesis, No. 18047, ETH Zurich, Switzerland, Zurich, 2008.
43. Simmons MJH, Zhu H, Bujalski W, Hewitt CJ, Nienow AW. Mixing in a model bioreactor using agitators with a high solidity ratio and deep blades. *Chem Eng Res Des.* 2007;85:551–559.
44. Coufort C, Derlon N, Ochoa-Chaves J, Line A, Paul E. Cohesion and detachment in biofilm systems for different electron acceptor and donors. *Water Sci Technol.* 2007;55:421–428.
45. Haut B, Ben Amor H, Coulon L, Jacquet A, Halloin V. Hydrodynamics and mass transfer in a Couette-Taylor bioreactor for the culture of animal cells. *Chem Eng Sci.* 2003;58:777–784.
46. Soos M, Moussa AS, Ehrl L, Sefcik J, Wu H, Morbidelli M. Effect of shear rate on aggregates size and morphology investigated under turbulent conditions in stirred tank. *J Colloid Interface Sci.* 2008;319:577–589.
47. Andereck CD, Liu SS, Swinney HL. Flow regimes in a circular Couette system with independently rotating cylinders. *J Fluid Mech.* 1986;164:155–183.
48. Kataoka K. *Taylor vortices and instabilities in circular Couette flows.* In: Cheremisinoff NP, editor. *Encyclopedia of Fluid Mechanics*, Vol.1. Houston: Gulf Publishing Company, 1986: 236–274.
49. Taylor GI. Stability of a viscous liquid contained between two rotating cylinders. *Philos Trans R Soc Lond A.* 1923;223:289–343.
50. Lueptow RM, Docter A, Min KY. Stability of axial-flow in an annulus with a rotating inner cylinder. *Phys Fluids A.* 1992;4:2446–2455.
51. Perry RH, Green DW. *Perry's Chemical Engineers' Handbook*. New York: McGraw-Hill, 1998.
52. Wendt G. Turbulente Strömung zwischen zwei rotierenden konaxialen Zylindern. *Ing Arch.* 1933;4:577–595.
53. Lathrop DP, Fineberg J, Swinney HL. Transition to shear-driven turbulence in Couette-Taylor flow. *Phys Rev A.* 1992;46:6390–6405.
54. Lewis GS, Swinney HL. Velocity structure functions, scaling, and transitions in high-Reynolds-number Couette-Taylor flow. *Phys Rev E.* 1999;59:5457–5467.

55. Blaser S. The hydrodynamical effect of vorticity and strain on the mechanical stability of flocs. PhD Thesis, No. 12851, ETH Zurich, Switzerland, Zurich, 1998.
56. Press WH, Teukolsky SA, Vetterling WT, Flannery BP. *Numerical Recipes in C: The Art of Scientific Computing*, 2nd ed. Cambridge: Cambridge University Press, 1992.
57. *FLUENT6.2*. UDF Manual. Fluent Inc., Canonsburg, PA, 2005.
58. Soos M, Ehrl L, Bäbler MU, Morbidelli M. Aggregate breakup in a contracting nozzle. *Langmuir*. 2010;26:10–18.
59. Hinze JO. Fundamentals of the hydrodynamic mechanism of splitting in dispersion processes. *AIChE J*. 1955;1:289–295.
60. *FLUENT6.2*. User's Guide. Fluent Inc., Canonsburg, PA, 2005.
61. Sengupta TK, Kabir MF, Ray AK. A Taylor vortex photocatalytic reactor for water purification. *Ind Eng Chem Res*. 2001;40:5268–5281.
62. Marchisio DL, Barresi AA, Fox RO. Simulation of turbulent precipitation in a semi-batch Taylor-Couette reactor using CFD. *AIChE J*. 2001;47:664–676.
63. Campolo M, Sbrizzai F, Soldati A. Time-dependent flow structures and Lagrangian mixing in Rushton-impeller baffled-tank reactor. *Chem Eng Commun*. 2003;58:1615–1629.
64. Kumaresan T, Joshi JB. Effect of impeller design on the flow pattern and mixing in stirred tanks. *Chem Eng J*. 2006;115:173–193.
65. Pope SB. *Turbulent Flows*. Cambridge: Cambridge University Press, 2000.
66. Cottet GH, Koumoutsakos P. *Vortex Methods—Theory and Practice*. New York: Cambridge University Press, 2000.
67. Monaghan JJ. An introduction to SPH. *Comput Phys Commun*. 1988;48:89–96.
68. Moussa AS, Soos M, Sefcik J, Morbidelli M. Effect of solid volume fraction on aggregation and breakage in colloidal suspensions in batch and continuous stirred tank. *Langmuir*. 2007;23:1664–1673.
69. Ehrl L, Soos M, Morbidelli M. Dependence of aggregate strength, structure, and light scattering properties on primary particle size under turbulent conditions in stirred tank. *Langmuir*. 2008;24:3070–3081.
70. Soos M, Moussa AS, Ehrl L, Sefcik J, Wu H, Morbidelli M. Dynamic response studies on aggregation and breakage dynamics of colloidal dispersions in stirred tanks. *J Dispersion Sci Technol*. 2008;29:605–610.
71. Sorensen CM. Light scattering by fractal aggregates: a review. *Aerosol Sci Technol*. 2001;35:648–687.
72. Kerker M. *The Scattering of Light and Other Electromagnetic Radiation*. New York: Academic Press, 1969.
73. Farias TL, Köylü ÖÜ, Carvalho MG. Range of validity of the Rayleigh-Debye-Gans theory for optics of fractal aggregates. *Appl Opt*. 1996;35:6560–6567.
74. Jones AR. Light scattering for particle characterization. *Prog Energy Combust Sci*. 1999;25:1–53.
75. Lambert S, Thill A, Ginestet P, Audic JM, Bottero JY. Structural interpretations of static light scattering patterns of fractal aggregates. I. Introduction of a mean optical index: numerical simulations. *J Colloid Interface Sci*. 2000;228:379–385.
76. Tishkovets VP, Petrova EV, Jockers K. Optical properties of aggregate particles comparable in size to the wavelength. *J Quant Spectrosc Radiat Transfer*. 2004;86:241–265.
77. Lattuada M, Ehrl L. Scattering properties of dense clusters of colloidal nanoparticles. *J Phys Chem B*. 2009;113:5938–5950.
78. Soos M, Lattuada M, Sefcik J. Interpretation of light scattering and turbidity measurements in aggregated systems: effect of intracluster multiple-light scattering. *J Phys Chem B*. 2009;113:14962–14970.
79. Petrova EV, Tishkovets VP, Jockers K. Polarization of light scattered by solar system bodies and the aggregate model of dust particles. *Sol Syst Res*. 2004;38:309–324.
80. Lattuada M, Wu H, Morbidelli M. A simple model for the structure of fractal aggregates. *J Colloid Interface Sci*. 2003;268:106–120.
81. Soos M, Sefcik J, Morbidelli M. Master curves for aggregation and gelation: effects of cluster structure and polydispersity. *Ind Eng Chem Res*. 2007;46:1709–1720.
82. Mandelbrot BB, Passoja DE, Paullay AJ. Fractal character of fracture surfaces of metals. *Nature*. 1984;308:721–722.
83. Lee C, Kramer TA. Prediction of three-dimensional fractal dimensions using the two-dimensional properties of fractal aggregates. *Adv Colloid Interface Sci*. 2004;112:49–57.
84. Ehrl L, Soos M, Lattuada M. Generation and geometrical analysis of dense clusters with variable fractal dimension. *J Phys Chem B*. 2009;113:10587–10599.
85. Desmet G, Verelst H, Baron GV. Local and global dispersion effects in Couette-Taylor flow. I. Description and modeling of the dispersion effects. *Chem Eng Sci*. 1996;51:1287–1298.
86. Snyder HA. Experiments on rotating flows between noncircular cylinders. *Phys Fluids*. 1968;11:1606–1611.
87. Zaccone A, Soos M, Lattuada M, Wu H, Bäbler MU, Morbidelli M. Breakup of dense colloidal aggregates under hydrodynamic stresses. *Phys Rev E*. 2009;79:061401.
88. Richardson LF. *Weather Prediction by Numerical Process*. Cambridge: Cambridge University Press, 1922.
89. Kolmogorov AN. The local structure of turbulence in incompressible viscous fluid for very large Reynolds numbers. Proceedings of the USSR Academy of Sciences, 1941;30:299–303 (Russian).
90. Kolmogorov AN. The local-structure of turbulence in incompressible viscous-fluid for very large Reynolds-numbers. *Proc R Soc London Ser A*. 1991;434:9–13.

Manuscript received Apr. 17, 2009, and revision received Dec. 9, 2009.